ELSEVIER

Contents lists available at ScienceDirect

# Results in Surfaces and Interfaces

journal homepage: www.elsevier.com/locate/rsurfi





# Grain engineering of solution-processed Sb<sub>2</sub>S<sub>3</sub> thin film by tuning precursor fabrication environments

Xiaomeng Duan, Al Amin, Yizhao Wang, Feng Yan

School for Engineering of Matter, Transport, and Energy, Arizona State University, Tempe, AZ, 85287, United States

#### ARTICLE INFO

Keywords: Grain engineering Sb<sub>2</sub>S<sub>3</sub> thin film Precursor solution environments Grain size

#### ABSTRACT

Antimony sulfide ( $Sb_2S_3$ ) has garnered significant attention recently due to its remarkable photovoltaic properties and low toxicity. However, the conventional physical vapor deposition approach faces challenges in achieving high-quality films due to  $Sb_2S_3$  having a quasi-one-dimensional nanoribbon structure. In contrast, solution-processed  $Sb_2S_3$  thin films have shown improved photovoltaic behavior, offering a low-cost and scalable fabrication method. Nonetheless, the sensitivity of the solution process to the chemical composition of the precursor poses a challenge, often requiring noble gas protection to prevent exposure to toxic solvents or moisture-sensitive chemicals. Despite this, the impact of precursor fabrication conditions on film growth behavior remains unexplored. In our study, we investigate how different processing atmospheres of precursors, namely nitrogen ( $N_2$ ) and air, affect grain growth and the associated optical and electronic performance of  $Sb_2S_3$  thin films. Our findings reveal that the presence of oxygen in the precursor can hinder grain growth by obstructing surface integration sites, resulting in undesired (hk0) orientation and even the formation of  $Sb_2O_3$  on the surface of the  $Sb_2S_3$  films, despite identical post-deposition conditions. This research sheds light on how the ambient conditions during precursor preparation can influence grain engineering, thereby providing valuable insights for controlling the grain size and producing high-quality  $Sb_2S_3$  absorber films.

# 1. Introduction

Antimony sulfide, i.e., Sb<sub>2</sub>S<sub>3</sub> thin film solar cell has garnered considerable attention, primarily due to its optimal bandgap (approximately 1.7 eV), high absorption coefficient (approximately  $1.8 \times 10^5$ cm<sup>-1</sup>), earth abundance, and environmentally friendly characteristics (Myagmarsereejid et al., 2021; Ning et al., 2021; Zheng et al., 2019; Cao et al., 2022a; Tao et al., 2019).  $Sb_2S_3$  has a quasi-one-dimensional structure with the unit of  $(Sb_4S_6)_n$  ribbons, determining photogenerated carriers transport rapidly along the (hk1) direction (Jin et al., 2020; Cao et al., 2022b; Pan et al., 2023). To date, several growth methods have been investigated to synthesize high-quality Sb<sub>2</sub>S<sub>3</sub> absorbers, including close space sublimation (Guo et al., 2019), spin coating (Kaienburg et al., 2018a), and hydrothermal method (Zhou et al., 2022). Especially, the physical vapor deposition of the Sb<sub>2</sub>S<sub>3</sub> possesses relatively lower performance for the solar cell device performance due to the challenges of controlling the grain orientation at a fast growth speed (Guo et al., 2019; Zhang et al., 2020; Du et al., 2022). Chemical solution approach stands out for its convenience, cost-effectiveness, and ease of upscale manufacturing.

Grain boundaries play a crucial role in governing the optoelectronic properties of polycrystalline optoelectronic materials (Fukuda et al., 2023; Hao et al., 2023). The presence of dangling bonds at grain boundaries can trap carriers, acting as nonradiative recombination centers. Therefore, it becomes imperative to increase grain size, as grain boundary densities can be minimized. However, grain growth behavior is difficult to control in Sb<sub>2</sub>S<sub>3</sub> absorbers (Liu et al., 2024). So far, it is reported that the introduction of the Ce ions in the Sb<sub>2</sub>S<sub>3</sub> precursors could significantly impact the grain growth and regulate the grain size of the Sb<sub>2</sub>S<sub>3</sub>, impacting the device performance (Liu et al., 2024). The nucleation and crystal growth of the film heavily depend on the in-situ chemical conditions of precursors for film deposition. For example, oxygen in the precursor plays a key role in regulating the crystallization process of materials, such as Nb<sub>3</sub>Sn(Sun et al., 2023) and graphene (Chuang and Woon, 2016). Most of the solution-processed Sb<sub>2</sub>S<sub>3</sub> films still need noble gas protection during the thin film growth, e.g., N2 gas-filled glovebox. How residual oxygen gas in the Sb<sub>2</sub>S<sub>3</sub> precursor impacts the grain growth behavior is unclear.

E-mail address: fengyan@asu.edu (F. Yan).

<sup>\*</sup> Corresponding author.

In this study, we investigate how the residual oxygen gas in the precursor impacts the  $Sb_2S_3$  grain growth and grain size. It is obtained that the introduction of oxygen in the precursors results in a smaller  $Sb_2S_3$  film grain size, undesired (hk0) grain orientation, and formation of  $Sb_2O_3$  on the surface. It indicates that oxygen molecules dissolved in the  $Sb_2S_3$  precursor could impede crystal growth by blocking surface integration sites, leading to a smaller grain size. These residual oxygen molecules also assist the formation of pinholes. This study provides valuable insights into the importance of controlling the precursor processing conditions for achieving large grain and pinhole-free  $Sb_2S_3$ , which is crucial for enhancing the performance of corresponding solar cells.

#### 2. Experimental

#### 2.1. Materials

 $Sb_2O_3$  (Alfa Aesar, 99.999%), Ethanol (Alfa Aesar, 94%–96%), Carbon disulfide (Alfa Aesar, 99.9%), and n-butylamine (Alfa Aesar, 98%) were purchased from Alfa Aesar and used without further purification.

# 2.2. Preparation of $Sb_2S_3$ precursor solutions

The precursors were prepared following the procedure previously reported, under ambient air and  $N_2$  conditions, respectively (Wang et al., 2017).  $Sb_2O_3$ , utilized as the antimony source, was dispersed within a

solution containing diluted carbon disulfide (CS<sub>2</sub>) in ethanol. Subsequently, n-butylamine was added dropwise to the mixed solution. Before use, the precursor was stirred in air and  $N_2$ , and indexed as  $Sb_2S_3$ -air and  $Sb_2S_3-N_2$ , respectively. To enhance the dissolution of oxygen in the solution, the precursor, prepared in the open air, was aerated by bubbling air during stirring. Solutions from both processing environments appeared clear and were fully dissolved, which rules out the possibility that the  $Sb_2O_3$  detected by XPS originates from the starting chemical. Note that both films from precursors prepared in air and  $N_2$  were annealed in the dry  $N_2$ -supplied glovebox to investigate the influence of precursor processing conditions.

# 2.3. Solar cell fabrication and characterization

Fabrication: F-doped SnO $_2$ -coated soda-lime glass (FTO) substrates were sequentially cleaned with detergent, acetone, isopropyl alcohol, and deionized water in an ultrasonic bath, with each step lasting 10 min. CdS window layers ( $\sim$ 100 nm) were then deposited on the cleaned FTO using the chemical bath deposition (CBD) method previously reported (Guo et al., 2018). The Sb $_2$ S $_3$  precursor, prepared in the air, was subsequently transferred to the dry N $_2$ -filled glovebox. Both precursors, prepared in air and N $_2$  were spin-coated onto the CdS-coated FTO substrate at 6000 rpm for 30 s, followed by pre-annealing at 200°C for 2 min and final annealing at 340°C for 2 min in the glovebox (O $_2$  and H $_2$ O < 0.1 ppm). The best crystallization conditions were optimized through 30 trials. The carbon electrodes were blade-coated with carbon paste (with

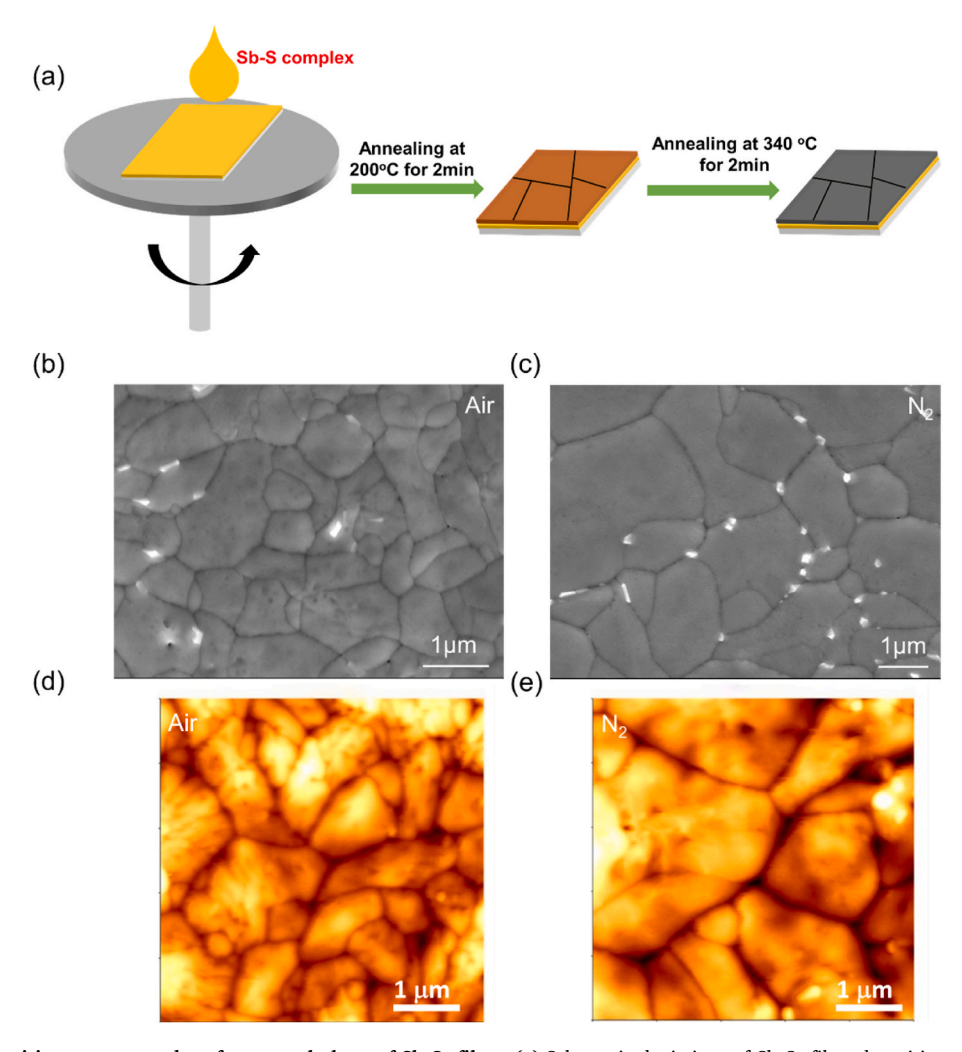


Fig. 1.  $Sb_2S_3$  films deposition process and surface morphology of  $Sb_2S_3$  films. (a) Schematic depictions of  $Sb_2S_3$  films deposition process. Scanning electron microscopy (SEM) of (b),  $Sb_2S_3$ -air and (c),  $Sb_2S_3$ -N<sub>2</sub> films. Atomic force microscopy (AFM) of (d),  $Sb_2S_3$ -air and (e),  $Sb_2S_3$ -N<sub>2</sub> films.

an active area of  $0.08~\rm cm^2)$  to form the solar cells. The highest device efficiencies in each case were identified over the course of the optimization of 20 devices. Throughout the following paragraphs, we will refer to these films as  $Sb_2S_3$ -air and  $Sb_2S_3$ -N<sub>2</sub> films, respectively.

Characterization: The structural characterization of the films was performed by X-ray diffraction (Philips X'Pert MPD) using Cu K $\alpha$  radiation ( $\lambda=1.5416$  Å) at a tube voltage of 45 kV and current of 40 mA. A scan speed of 6.79°/min was employed to collect the XRD data (20 range  $=10\text{-}70^\circ\text{-})$ . The X-Ray instrument is equipped with a goniometer for angular movement.

Film morphology was determined using scanning electron microscope (SEM, JEOL 7000 FE) and atomic force microscopy (AFM, Park XE70). SEM images were obtained using the JEOL 7000 FE-SEM (Tokyo, Japan) at 15 000  $\times$  magnification, with a working distance of 10.0 mm and an accelerating voltage of 10.0 kV in the SE imaging mode. The AFM topography was obtained in contact mode through a Pt/Ir coated contact probe (ANSCM-PT from AppNano, Inc.). The cantilever spring constant was around 3N/m, and resonance frequency was  $\sim\!60$  kHz. AFM images were collected in FMM head mode with a scan rate of 1 Hz.

The chemical oxidation states of the  $Sb_2S_3$  films were analyzed using X-ray photoelectron spectroscopy (XPS) on the Kratos Axis DLD spectrometer equipped with a monochromatic Al K $\alpha$  source (h $\nu=1486.6$  eV) under a vacuum of  $10^{-10}$  Torr. The sample charging issues were calibrated using the standard carbon peak C 1s (284.8 eV) as a reference. Peak fitting and deconvolution were conducted by CasaXPS software, using Lorentzian Asymmetric lineshape and Shirley background subtraction. Survey spectra were acquired in the BE range of 1200–0 eV at room temperature, with an analyzer pass energy of 160 eV and an energy step size of 1 eV. High-resolution spectra were obtained with a pass energy of 20 eV and a step size of 0.1 eV.

The absorber layer's light absorbance and transmittance spectra were measured using a UV–Vis spectrometer (Shimadzu UV-1800) over a wavelength range from 300 nm to 1100 nm, with a step size of 10 nm.

Current density-voltage (J-V) characteristics were measured by the Newport Sol3A class AAA solar simulator (Oriel, model 94023 A; Newport Corporation, Irvine, CA, USA) under ambient conditions (room temperature, 1000 W/m, air mass 1.5-G illumination). A Keithley 2420 source meter (Keithley Instrument Inc.) was used to acquire J-V characteristics. A calibrated Si-reference cell and meter (Newport, 91150 V, certified by NREL) were used to calibrate the solar simulator prior to the measurement. The voltage was swept from  $-0.2\ V$  to  $1.2\ V$  with  $101\ Sweep$  points and a dwell time of  $10\ ms$ .

External quantum efficiency (EQE) of solar cells was measured using a solar cell spectral response measurement system (QE-T, Enli Technology, Co. Ltd). Measurements were taken over a wavelength range from 300 nm to 1100 nm with a step size of 10 nm. The data collection involved 8000 sampling points at a sample rate of 15.

# 3. Results and discussion

The deposition process of Sb<sub>2</sub>S<sub>3</sub> films is illustrated schematically in Fig. 1a. Both the precursors prepared in N<sub>2</sub> and air (as detailed in the materials and methods section) were transferred into the N2-filled glovebox and spin-coated on the substrate. The films were then annealed at 200°C for solvent drying, followed by high-temperature annealing at 340 °C for 2 min to promote crystal growth. Fig. 1b-c displays the surface morphology of Sb<sub>2</sub>S<sub>3</sub>-air and Sb<sub>2</sub>S<sub>3</sub>-N<sub>2</sub> films, as analyzed by scanning electron microscopy (SEM). It is shown that the Sb<sub>2</sub>S<sub>3</sub>-air film showed a grain size of  $\sim 1 \mu m$  while Sb<sub>2</sub>S<sub>3</sub>-N<sub>2</sub> film has a much larger grain size (~2 or 3 µm). The AFM images (Fig. 1d-e) also indicate a larger grain size for the Sb<sub>2</sub>S<sub>3</sub>–N<sub>2</sub> film, with a root mean square (RMS) roughness of ~16.23 nm, whereas the Sb<sub>2</sub>S<sub>3</sub>-air film exhibits an RMS roughness  $\sim 19.82$  nm. The grain orientation of Sb<sub>2</sub>O<sub>3</sub> differs from that of Sb<sub>2</sub>S<sub>3</sub>, which could be a contributing factor to the high surface roughness observed in the Sb<sub>2</sub>S<sub>3</sub>-air film. The potential chemical reactions involved in the formation of Sb<sub>2</sub>S<sub>3</sub> are listed below:

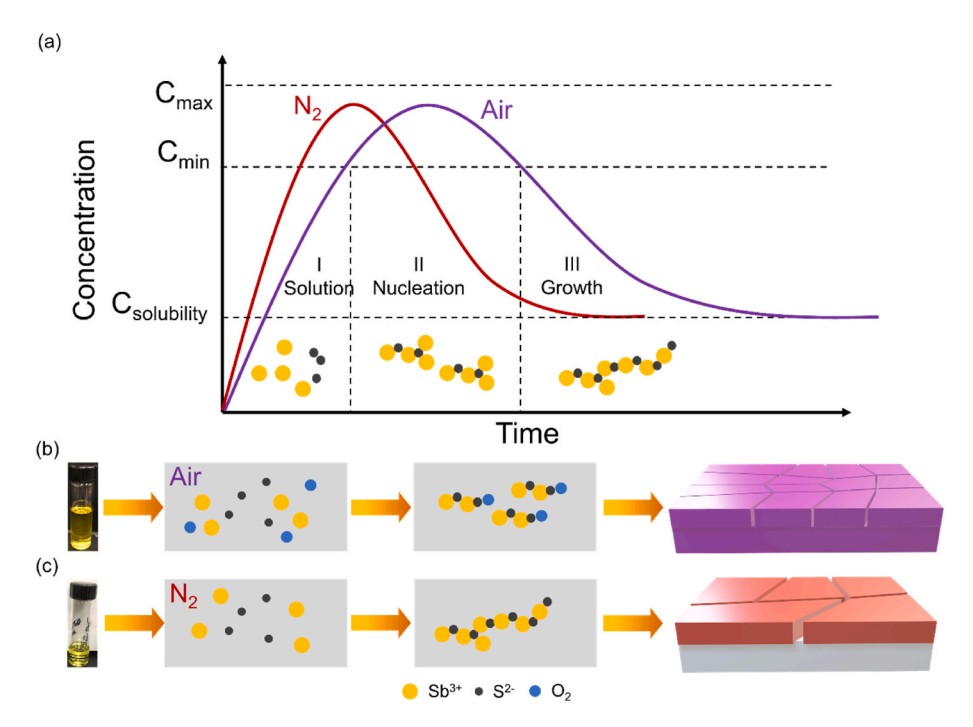


Fig. 2. Crystal growth of  $Sb_2S_3$ -Air and  $Sb_2S_3$ -N<sub>2</sub> films. (a) LaMer diagram illustrates the generation of atoms, nuclei, and the subsequent growth of the nuclei. Schematic illustrations depict the growth of (b),  $Sb_2S_3$ -Air thin film and (c),  $Sb_2S_3$ -N<sub>2</sub> thin film.

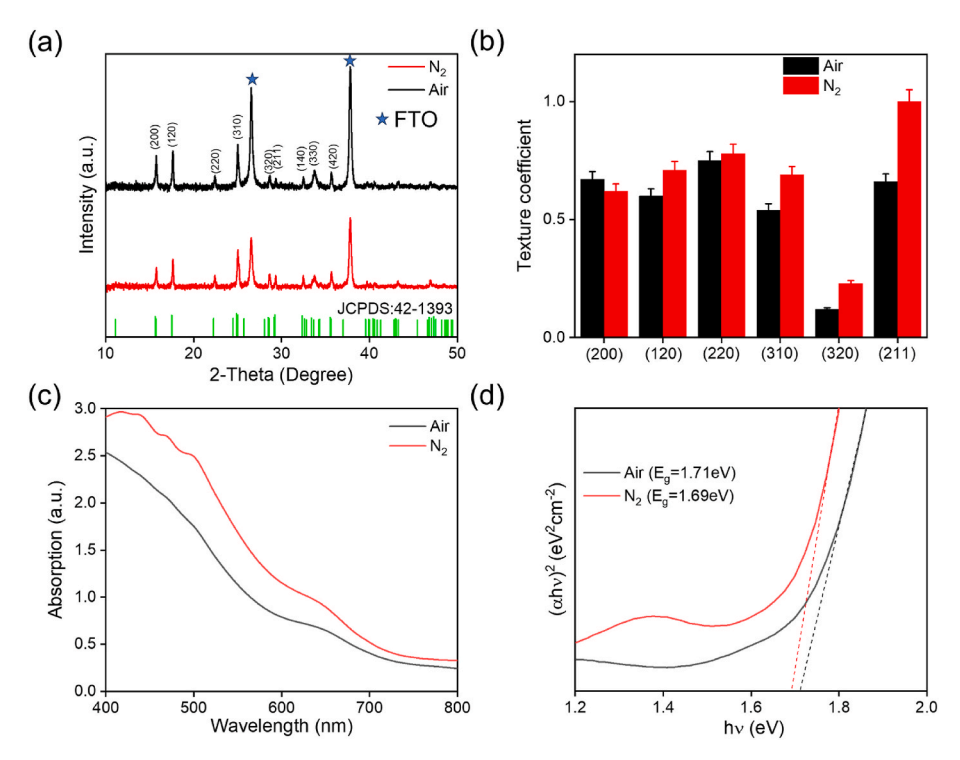


Fig. 3. Grain orientation and bandgap of  $Sb_2S_3$ - $N_2$  and  $Sb_2S_3$ -air films. (a), X-ray diffraction (XRD) patterns of  $Sb_2S_3$ - $N_2$  and  $Sb_2S_3$ -air films. (b), Texture coefficient of  $Sb_2S_3$  films calculated from XRD results. The error bar represents 95% confidence limit. (c), Absorption spectra and (d), Tauc plot of  $Sb_2S_3$ -air and  $Sb_2S_3$ - $N_2$  films.

The Sb complex will decompose into  $\mathrm{Sb}_2\mathrm{S}_3$  at high temperatures. The nucleation and crystal growth can be described by the LaMer model, as exhibited in Fig. 2a. After the spin-coating process, during low-temperature annealing, the concentration of precursors increases, approaching supersaturation concentration where nucleation begins (Stage I). Nuclei grow with the diffusion of precursor solutes (Stage II). When the solute is consumed faster than the evaporation of the

precursor solvent, the concentration falls below supersaturation concentration, leading to the exclusive growth of nuclei without the formation of new nuclei (Stage III) (Abbas et al., 2020). The oxygen molecules in the  $\mathrm{Sb}_2\mathrm{S}_3$ -Air precursor serve as impurities, suppressing crystal growth by blocking integration sites (Derdour et al., 2011). Detailed crystal growth mechanisms are shown in Fig. 2b and c. In the presence of oxygen in the precursor, the diffusion rate of the solute may

Table 1 Texture coefficient of  $Sb_2S_3-N_2$  and  $Sb_2S_3$ -air films with normalization.

	(200)	(120)	(220)	(310)	(320)	(211)
Sb <sub>2</sub> S <sub>3</sub> –N <sub>2</sub> film	0.62	0.71	0.78	0.69	0.23	1
$Sb_2S_3$ – $N_2$ film error bar ( $\pm$ )	0.03	0.04	0.04	0.04	0.01	0.05
Sb <sub>2</sub> S <sub>3</sub> -Air film	0.67	0.60	0.75	0.54	0.12	0.66
$\mathrm{Sb}_2\mathrm{S}_3$ -Air film error bar ( $\pm$ )	0.03	0.03	0.04	0.03	0.01	0.03

slow down, leading to predominance of the nucleation process. Conversely, when the precursor lacks oxygen, slow solvent evaporation occurs along with a rapid diffusion rate of the solute, leading to a larger grain size in  $Sb_2S_3$ – $N_2$  (Abbas et al., 2020). In addition, the  $Sb_2S_3$ – $N_2$  film displayed fewer pinholes than that of the  $Sb_2S_3$ -Air film as shown in Fig. 1b and c. The formation of pinholes in the  $Sb_2S_3$ -Air film is attributed to the introduction of oxygen during precursor preparation, which may trigger a degassing process during film growth, leading to the formation of pinholes (Hao et al., 2020). However, fewer pinholes still exist in the  $Sb_2S_3$ – $N_2$  film. That is possibly due to rapid annealing, lasting only for 2 min, resulting in incomplete crystallization of the film. Moreover, lots of white particles observed along the grain boundaries observed in both films are likely residual nuclei of  $Sb_2S_3$  resulting from the crystal growth process (Wang et al., 2017).

Fig. 3a presents the X-ray diffraction (XRD) patterns of  $Sb_2S_3$ -Air and  $Sb_2S_3$ -N<sub>2</sub> films deposited on FTO/CdS substrates. Both  $Sb_2S_3$ -Air and  $Sb_2S_3$ -N<sub>2</sub> films show the presence of the  $Sb_2S_3$  phase without a secondary phase. The calculated texture coefficient based on the XRD results is exhibited in Fig. 3b, where the  $Sb_2S_3$ -N<sub>2</sub> film exhibits stronger intensity in (hk1) peaks, such as (211), indicating that the ( $Sb_4S_6$ )n ribbons tend to grow normal to the substrate, while the  $Sb_2S_3$ -Air film shows less intensity in (hk1) orientation. The detailed texture coefficient for the films are shown in Table 1 The various growth behavior observed in  $Sb_2S_3$  films may originate from the presence of oxygen incorporated into the precursor solution, which can impact the growth process. The optical absorption of  $Sb_2S_3$  films was characterized using UV-Vis

spectroscopy as shown in Fig. 3c. Sb<sub>2</sub>S<sub>3</sub>-N<sub>2</sub> film demonstrates better light absorption across all wavelengths, potentially due to its dense, pinhole-free morphology and large grain size compared to Sb<sub>2</sub>S<sub>3</sub>-air film, as shown in Fig. 1. Due to the phenomenon of grain boundary scattering (Kimmer et al., 2007; Henriquez et al., 2013), photons are more likely to be scattered in films with small grain sizes (Sb<sub>2</sub>S<sub>3</sub>-air film) compared to those with larger grain sizes (Sb<sub>2</sub>S<sub>3</sub>-N<sub>2</sub> film). Consequently, less light would be absorbed by the Sb<sub>2</sub>S<sub>3</sub>-air film. The bandgap of Sb<sub>2</sub>S<sub>3</sub>-air and Sb<sub>2</sub>S<sub>3</sub>-N<sub>2</sub> films are determined as 1.71eV and 1.69eV, respectively, using Tauc fitting (Fig. 3d). These values are in good agreement with the reported results (Cai et al., 2020). The incorporation of oxygen in the precursor solution results in the formation of oxygen associated defects in the resulting Sb<sub>2</sub>S<sub>3</sub> film (Cai et al., 2020; Lian et al., 2021; Kondrotas et al., 2018), altering lattice constants of the Sb<sub>2</sub>S<sub>3</sub>, potentially explaining the discrepancy in bandgap observed between Sb<sub>2</sub>S<sub>3</sub>-N<sub>2</sub> and Sb<sub>2</sub>S<sub>3</sub>-air films.

To investigate the chemical composition differences between  $Sb_2S_3$ -air and  $Sb_2S_3-N_2$  films, X-ray photoelectron spectroscopy (XPS) was carried out. The Sb 3 d spectra of  $Sb_2S_3-N_2$  and  $Sb_2S_3$ -air films are illustrated in Fig. 4a and c, respectively. The  $Sb_2S_3$ -Air film exhibits double peaks at 528.5 eV and 537.9 eV, which are attributed to Sb  $3d_{5/2}$  and Sb  $3d_{3/2}$ , respectively, originating from the Sb–S bond (Jiang et al., 2019). Additional peaks at 529.7 eV and 539.1eV are identified as the

**Table 2** Photovoltaic average of solar cells fabricated with  $Sb_2S_3$ -air and  $Sb_2S_3$ - $N_2$  films measured under one Sun AM 1.5G illumination. In each condition, cell number -5

Device	V <sub>oc</sub> (V)	J <sub>sc</sub> (mA/ cm <sup>2</sup> )	Fill Factor (%)	PCE (%) $R_s$ ( $\Omega$ cm <sup>2</sup> ) $R_{sh}$ ( $\Omega$ cm <sup>2</sup> )
Sb <sub>2</sub> S <sub>3</sub> -air	$\begin{array}{c} \textbf{0.31} \pm \\ \textbf{0.07} \end{array}$	$5.79 \pm \\ 0.23$	$31.49 \pm \\3.94$	$\begin{array}{c} 0.57 \pm 0.2\ 31.50 \pm 2.82 \\ 85.26 \pm 3.14 \end{array}$
$Sb_2S_3-N_2$	$\begin{array}{l} \textbf{0.49} \pm \\ \textbf{0.058} \end{array}$	$\begin{array}{c} 6.67 \pm \\ 0.35 \end{array}$	$32.63 \pm 2.36$	$\begin{array}{c} 1.07 \pm 0.16 \ 50.67 \pm 2.81 \\ 102.41 \ \pm 2.94 \end{array}$

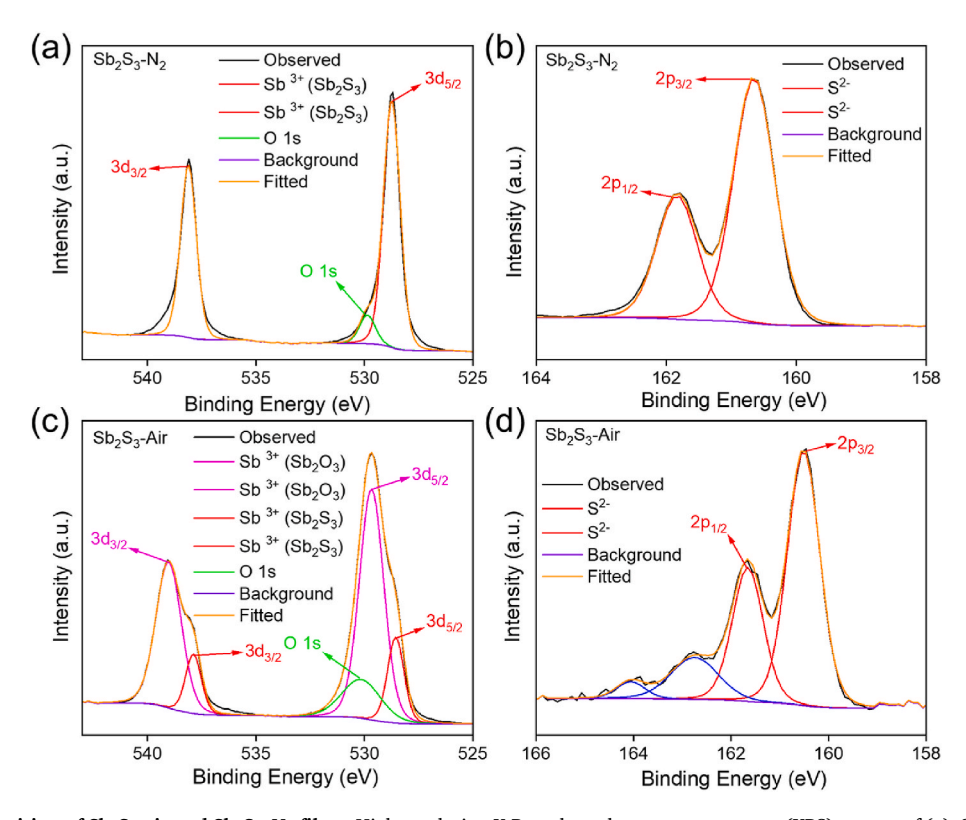


Fig. 4. Chemical composition of Sb<sub>2</sub>S<sub>3</sub>-air and Sb<sub>2</sub>S<sub>3</sub>-N<sub>2</sub> films. High-resolution X-Ray photoelectron spectroscopy (XPS) spectra of (a), Sb 3 d and (b), S 2p peaks of Sb<sub>2</sub>S<sub>3</sub>-N<sub>2</sub> film. (c), Sb 3 d and (d), S 2p peaks of Sb<sub>2</sub>S<sub>3</sub>-air film.

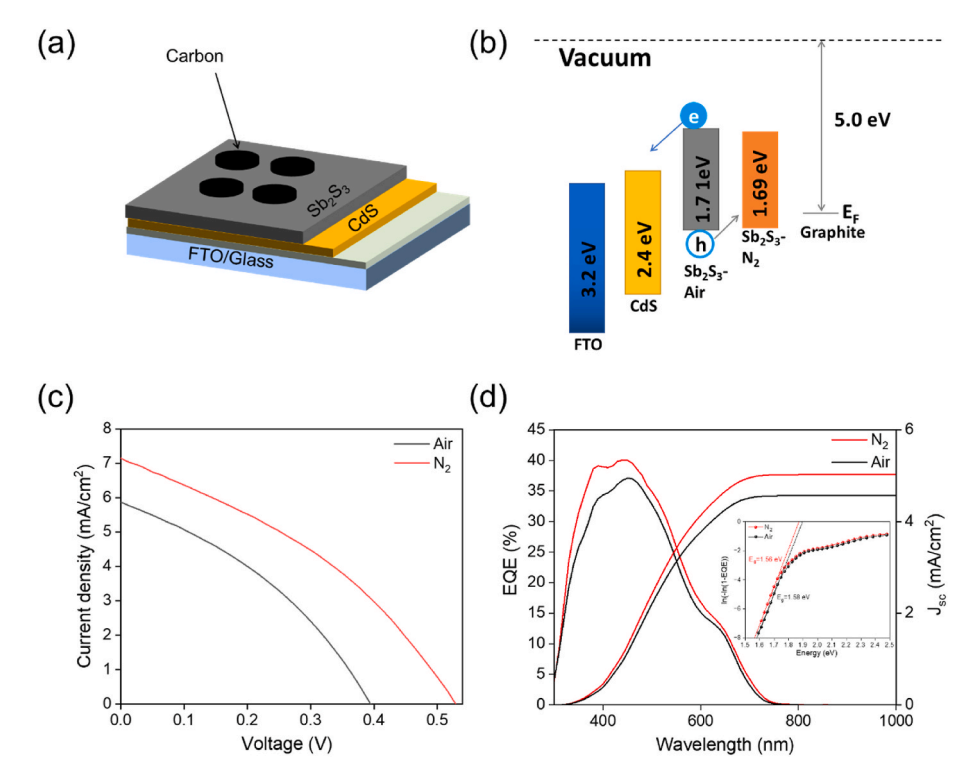


Fig. 5. Device configuration and device performance characterizations. (a), Schematics of a typical device structure. (b), Energy level band alignment of the device. (c), Current density-voltage curves and (d), external quantum efficiency (EQE) spectra of devices fabricated with  $Sb_2S_3$ -air and  $Sb_2S_3$ -N<sub>2</sub> films. Inset figure illustrates the bandgap derived from the EQE spectra of the devices.

Sb–O band, suggesting the presence of  $Sb_2O_3$  in the  $Sb_2S_3$ -Air film (Han et al., 2020). The S 2p peak fitting displays two peaks located at a binding energy of 160.6eV and 161.8eV, corresponding to  $2p_{3/2}$  and  $2p_{1/2}$ , respectively, for both  $Sb_2S_3$ -air and  $Sb_2S_3$ -N<sub>2</sub> films (Jiang et al., 2019). The formation of  $Sb_2O_3$  in the  $Sb_2S_3$ -air film may result from the presence of dissolved oxygen in the precursor, given that both the  $Sb_2S_3$ -air film and  $Sb_2S_3$ -N<sub>2</sub> film were annealed in the dry N<sub>2</sub>-filled glovebox. This observation provides evidence that the formation of  $Sb_2S_3$  film is sensitive to the precursor fabrication conditions.

To understand how grain engineering impacts the electrical behavior in Sb<sub>2</sub>S<sub>3</sub> film-based solar cells, we fabricated simple solar cell devices using both Sb<sub>2</sub>S<sub>3</sub>-Air and the Sb<sub>2</sub>S<sub>3</sub>-N<sub>2</sub> films (see Table 2). Note that the device architecture was simplified to FTO/CdS/Sb<sub>2</sub>S<sub>3</sub>/Carbon electrode, as shown in Fig. 5a. The band alignment for the device is displayed in Fig. 5b (Guo et al., 2019), where the bandgap of the Sb<sub>2</sub>S<sub>3</sub>-air and Sb<sub>2</sub>S<sub>3</sub>-N<sub>2</sub> films differs, potentially leading to various carrier extraction. Current density-voltage (J-V) curves under one Sun AM 1.5G illumination are presented in Fig. 5c. Detailed device performance of solar cells fabricated with the Sb<sub>2</sub>S<sub>3</sub>-N<sub>2</sub> and Sb<sub>2</sub>S<sub>3</sub>-air films is listed in Table 2. The device fabricated with Sb<sub>2</sub>S<sub>3</sub>-N<sub>2</sub> film exhibits a highest power conversion efficiency (PCE) of 1.35% with a  $V_{oc}$  of 0.54 V,  $J_{sc}$  of 7.14 mA/cm<sup>2</sup>, and a fill factor (FF) of 35.01%, while the device with Sb<sub>2</sub>S<sub>3</sub>-air absorber demonstrates a highest PCE of 0.82%, a  $V_{oc}$  of 0.39 V, a  $J_{sc}$  of 5.87  $mA/cm^2,$  and an FF of 35.84%. The increase in  $V_{oc}$  and  $J_{sc}$  of the Sb<sub>2</sub>S<sub>3</sub>–N<sub>2</sub> device can be associated with the pinhole-free morphology, as shown in Fig. 1. These pinholes on the Sb<sub>2</sub>S<sub>3</sub>-air film may act as recombination centers, negatively impacting device performance due to direct contact between the back contact and electron transport layer (Zhang et al., 2023). Additionally, the larger grain size of the Sb<sub>2</sub>S<sub>3</sub>-N<sub>2</sub> film may also reduce the grain boundary density and consequently reduce carrier recombination in the film (Kim et al., 2016). Moreover, (Sb<sub>4</sub>Se<sub>6</sub>)<sub>n</sub> nanoribbons grown with (hk1) planes may also facilitate carrier transport along the ribbons, promoting the improved device performance (Zhou et al., 2015; Peng et al., 2023). However, the device fabricated with Sb<sub>2</sub>S<sub>3</sub>-N<sub>2</sub> film exhibits a slightly lower FF, and enhanced

series resistance. While fewer pinholes are present in the Sb<sub>2</sub>S<sub>3</sub>–N<sub>2</sub> film, the series resistance of the corresponding device increases, and the parallel resistance of the device increases. The direct contact between the buffer layer and the back contact, facilitated by pinholes in the absorber, could create current paths, potentially compromising device performance. However, the extent of loss paths depends on the combinations of buffer layer and back contact (Kaienburg et al., 2018b). Therefore, passivating pinholes in the film may not ensure a significant enhancement in the fill factor of the device. External quantum efficiency (EQE) results in Fig. 5d illustrate that the device fabricated with Sb<sub>2</sub>S<sub>3</sub>-N<sub>2</sub> film exhibits better photon response. The significantly lower current density observed in the EQE spectra compared to the I-V curves can be attributed to the different wavelength ranges between the AAA solar simulator for the IV and EQE measurements, and the rough interface between the light absorber and the porous carbon electrode (Amin et al., 2023; Dalal and Moore, 1977; Dalal and Rothwarf, 1979; 1). Bandgap was also determined from the EQE spectra and incorporated into the inset of Fig. 5d. According to the equation ln (-ln (1-EQE))∝  $(E-E_g)/E_U$  (Li et al., 2019; Hages et al., 2016), where  $E_g$  represents the bandgap, the intercept with the X-axis corresponds to the bandgap. The bandgaps of the Sb<sub>2</sub>S<sub>3</sub>-Air and Sb<sub>2</sub>S<sub>3</sub>-N<sub>2</sub> films were 1.58 eV and 1.56 eV, respectively. Results from both EQE spectra and Tauc fitting indicate that the Sb<sub>2</sub>S<sub>3</sub>-Air film exhibits a slightly larger bandgap. As a result, a blue shift was observed in the Sb<sub>2</sub>S<sub>3</sub>-Air device in the EQE spectra compared to the Sb<sub>2</sub>S<sub>3</sub>–N<sub>2</sub> device.

#### 4. Conclusions

In summary, our work reveals that controlling oxygen during the precursor preparation step significantly influences the grain size, grain orientation, and chemical composition of  $Sb_2S_3$  films, consequently impacting the performance of the corresponding solar cells. The  $Sb_2S_3$ – $N_2$  film shows a larger grain size with a smooth surface, ensuring a better junction quality.  $Sb_2S_3$ – $N_2$  film prefers (hk) orientation, which is beneficial for carrier transport. Additionally, oxygen is introduced and

converted into the  $Sb_2O_3$  during film annealing.  $Sb_2S_3$ – $N_2$  solar cell exhibits a better PCE of 1.35%, which reflected the improved  $Sb_2S_3$  film quality. Therefore, this work provides evidence that the control of oxygen in the  $Sb_2S_3$  precursor significantly impacts the quality of the resulting  $Sb_2S_3$  film. This study offers valuable insights into a novel approach for regulating grain engineering in  $Sb_2S_3$ , leading to enhanced film quality. These findings hold significant promise for the development of highly efficient  $Sb_2S_3$  solar cells.

# CRediT authorship contribution statement

Xiaomeng Duan: Writing – original draft, Methodology. Al Amin: Writing – review & editing, Methodology. Yizhao Wang: Writing – review & editing. Feng Yan: Writing – review & editing, Project administration, Funding acquisition, Conceptualization.

# Declaration of competing interest

The authors declare that they have no known competing financial interests or personal relationships that could have appeared to influence the work reported in this paper.

# Data availability

Data will be made available on request.

# Acknowledgments

This work is supported by the United State National Science Foundation under contract No. ECCS-2413632, MOMS-2330728, TI-2329871, and DMR-2330738, and CMMI-2226918, and DMREF-2323766.

#### References

- Abbas, M., Zeng, L., Guo, F., Rauf, M., Yuan, X.-C., Cai, B., 2020. A critical review on crystal growth techniques for scalable deposition of photovoltaic perovskite thin films. Materials 13, 4851.
- Amin, A., Duan, X., Wall, J., Khawaja, K.A., Xiang, W., Li, L., Yan, F., 2023. Heterostructured CdS buffer layer for Sb2Se3 thin film solar cell. Sol. RRL 7, 2300417
- 1 Amin, A., Duan, X., Zhao, K., Khawaja, K., Xiang, W., Qian, X., Yan, F., 2024. Solution-processed Sb2 (S, Se) 3 seeds-assisted Sb2Se3 thin film growth for high efficiency solar cell. Sol. RRL 8, 202400151.
- Cai, Z., Dai, C.-M., Chen, S., 2020. Intrinsic defect limit to the electrical conductivity and a two-step p-type doping strategy for overcoming the efficiency bottleneck of Sb2S3based solar cells. Sol. RRL 4, 1900503.
- Cao, Y., Liu, C., Yang, T., Zhao, Y., Na, Y., Jiang, C., Zhou, J., Pang, J., Liu, H., Rummeli, M.H., 2022a. Gradient bandgap modification for highly efficient carrier transport in antimony sulfide-selenide tandem solar cells. Sol. Energy Mater. Sol. Cell. 246, 111926.
- Cao, Y., Qu, P., Wang, C., Zhou, J., Li, M., Yu, X., Yu, X., Pang, J., Zhou, W., Liu, H., 2022b. Epitaxial growth of vertically aligned antimony selenide nanorod arrays for heterostructure based self-powered photodetector. Adv. Opt. Mater. 10, 2200816.
- Chuang, M.-C., Woon, W.-Y., 2016. Nucleation and growth dynamics of graphene on oxygen exposed copper substrate. Carbon 103, 384–390.
- Dalal, V.L., Moore, A.R., 1977. Design considerations for high-intensity solar cells. J. Appl. Phys. 48, 1244–1251.
- Dalal, V.L., Rothwarf, A., 1979. Comment on 'A simple measurement of absolute solar cell efficiency'. J. Appl. Phys. 50, 2980–2981.
- Derdour, L., Pack, S., Skliar, D., Lai, C., Kiang, S., 2011. Crystallization from solutions containing multiple conformers: a new modeling approach for solubility and supersaturation. Chem. Eng. Sci. 66, 88–102.
- Du, Y., Liu, F., Jiang, L., Jia, M., Zhang, Z., 2022. Ultra-fine Sb2S3 particles encapsulated in activated-carbon: a high-performance anode for Li-ion batteries. J. Alloys Compd. 907, 164469.
- Fukuda, R., Nishimura, T., Yamada, A., 2023. Experimental and theoretical EBIC analysis for grain boundary and CdS/Cu (In, Ga) Se2 heterointerface in Cu (In, Ga) Se2 solar cells. Prog. Photovoltaics Res. Appl. 31, 678–689.
- Guo, L., Zhang, B., Qin, Y., Li, D., Li, L., Qian, X., Yan, F., 2018. Tunable quasi-one-dimensional ribbon enhanced light absorption in Sb2Se3 thin-film solar cells grown by close-space sublimation. Sol. RRL 2, 1800128.

- Guo, L., Zhang, B., Li, S., Zhang, Q., Buettner, M., Li, L., Qian, X., Yan, F., 2019. Scalable and efficient Sb2S3 thin-film solar cells fabricated by close space sublimation. Apl. Mater. 7.
- Hages, C.J., Koeper, M.J., Agrawal, R., 2016. Optoelectronic and material properties of nanocrystal-based CZTSe absorbers with Ag-alloying. Sol. Energy Mater. Sol. Cell. 145, 342–348.
- Han, Q., Sun, Y., Zhang, W., Li, X., Li, Y., Zhang, X., Deng, Y., 2020. Synthesis of onedimensional yolk-shell Sb 2 O 3/TiO 2 composite as an anode material for enhanced lithium-storage properties. Ionics 26, 1221–1228.
- Hao, L., Li, Z., Wang, L., Liu, R., Shao, Z., Zhou, Z., Guo, X., Cui, G., Liu, S.F., Pang, S., 2020. A temperature gradient-induced directional growth of a perovskite film. J. Mater. Chem. A 8, 17019–17024.
- Hao, M., Duan, T., Ma, Z., Ju, M.G., Bennett, J.A., Liu, T., Guo, P., Zhou, Y., 2023. Flattening grain-boundary grooves for perovskite solar cells with high optomechanical reliability. Adv. Mater. 35, 2211155.
- Henriquez, R., Flores, M., Moraga, L., Kremer, G., González-Fuentes, C., Munoz, R.C., 2013. Electron scattering at surfaces and grain boundaries in thin Au films. Appl. Surf. Sci. 273, 315–323.
- Jiang, C., Tang, R., Wang, X., Ju, H., Chen, G., Chen, T., 2019. Alkali metals doping for high-performance planar heterojunction Sb2S3 solar cells. Sol. RRL 3, 1800272.
- Jin, X., Fang, Y., Salim, T., Feng, M., Hadke, S., Leow, S.W., Sum, T.C., Wong, L.H., 2020. In situ growth of [hk1]-oriented Sb2S3 for solution-processed planar heterojunction solar cell with 6.4% efficiency. Adv. Funct. Mater. 30, 2002887.
- Kaienburg, P., Klingebiel, B., Kirchartz, T., 2018a. Spin-coated planar Sb2S3 hybrid solar cells approaching 5% efficiency. Beilstein J. Nanotechnol. 9, 2114–2124.
- Kaienburg, P., Hartnagel, P., Pieters, B.E., Yu, J., Grabowski, D., Liu, Z., Haddad, J., Rau, U., Kirchartz, T., 2018b. How contact layers control shunting losses from pinholes in thin-film solar cells. J. Phys. Chem. C 122, 27263–27272.
- Kim, H.D., Ohkita, H., Benten, H., Ito, S., 2016. Photovoltaic performance of perovskite solar cells with different grain sizes. Adv. Mater. 28, 917–922.
- Kimmer, C., Aubry, S., Skye, A., Schelling, P.K., 2007. Scattering of phonons from a high-energy grain boundary in silicon: dependence on angle of incidence. Phys. Rev. B 75, 144105.
- Kondrotas, R., Chen, C., Tang, J., 2018. Sb2S3 solar cells. Joule 2, 857-878.
- Li, X., Zhuang, D., Zhang, N., Zhao, M., Yu, X., Liu, P., Wei, Y., Ren, G., 2019. Achieving 11.95% efficient Cu 2 ZnSnSe 4 solar cells fabricated by sputtering a Cu–Zn–Sn–Se quaternary compound target with a selenization process. J. Mater. Chem. A 7, 9948–9957.
- Lian, W., Jiang, C., Yin, Y., Tang, R., Li, G., Zhang, L., Che, B., Chen, T., 2021. Revealing composition and structure dependent deep-level defect in antimony trisulfide photovoltaics. Nat. Commun. 12, 3260.
- Liu, X., Cai, Z., Wan, L., Xiao, P., Che, B., Yang, J., Niu, H., Wang, H., Zhu, J., Huang, Y. T., 2024. Grain engineering of Sb2S3 thin films to enable efficient planar solar cells with high open-circuit voltage. Adv. Mater. 36, 2305841.
- Myagmarsereejid, P., Ingram, M., Batmunkh, M., Zhong, Y.L., 2021. Doping strategies in Sb2S3 thin films for solar cells. Small 17, 2100241.
- Ning, H., Guo, H., Zhang, J., Wang, X., Jia, X., Qiu, J., Yuan, N., Ding, J., 2021. Enhancing the efficiency of Sb2S3 solar cells using dual-functional potassium doping. Sol. Energy Mater. Sol. Cell. 221, 110816.
- Pan, X., Pan, Y., Shen, L., Wang, L., Wang, R., Weng, G., Jiang, J., Hu, X., Chen, S., Yang, P., 2023. All-vacuum-processed Sb2 (S, Se) 3 thin film photovoltaic devices via controllable tuning seed orientation. Adv. Funct. Mater. 33, 2214511.
- Peng, Z., Zheng, Q., Wang, R., Sun, L., Wang, H., Yuan, Y., Xing, Y., Yao, L., Bi, J., Li, W., 2023. Controllable (hk 1) preferred orientation of Sb2S3 thin films fabricated by pulse electrodeposition. Sol. Energy Mater. Sol. Cell. 253, 112208.
- Sun, Z., Dare, D.K., Baraissov, Z., Muller, D.A., Thompson, M.O., Liepe, M.U., 2023. Thermodynamic route of Nb3Sn nucleation: role of oxygen. Apl. Mater. 11.
- Tao, J., Hu, X., Guo, Y., Hong, J., Li, K., Jiang, J., Chen, S., Jing, C., Yue, F., Yang, P., 2019. Solution-processed SnO2 interfacial layer for highly efficient Sb2Se3 thin film solar cells. Nano Energy 60, 802–809.
- Wang, X., Li, J., Liu, W., Yang, S., Zhu, C., Chen, T., 2017. A fast chemical approach towards Sb 2 S 3 film with a large grain size for high-performance planar heterojunction solar cells. Nanoscale 9, 3386–3390.
- Zhang, H., Yuan, S., Deng, H., Ishaq, M., Yang, X., Hou, T., Shah, U.A., Song, H., Tang, J., 2020. Controllable orientations for Sb2S3 solar cells by vertical VTD method. Prog. Photovoltaics Res. Appl. 28, 823–832.
- Zhang, L., Xiao, P., Che, B., Yang, J., Cai, Z., Wang, H., Gao, J., Liang, W., Wu, C., Chen, T., 2023. Mechanistic study of the transition from antimony oxide to antimony sulfide in the hydrothermal process to obtain highly efficient solar cells. ChemSusChem 16, e202202049.
- Zheng, Q., Wang, C., Ma, G., Jin, M., Cheng, S., Lai, Y., Yu, J., 2019. Annealing temperature impact on Sb2S3 solar cells prepared by spin-coating method. Mater. Lett. 243, 104–107.
- Zhou, Y., Wang, L., Chen, S., Qin, S., Liu, X., Chen, J., Xue, D.-J., Luo, M., Cao, Y., Cheng, Y., 2015. Thin-film Sb2Se3 photovoltaics with oriented one-dimensional ribbons and benign grain boundaries. Nat. Photonics 9, 409–415.
- Zhou, J., Tang, Z., Yang, T., Meng, D., Chi, K., Cai, Y., Cao, Y., Yu, X., Yu, X., Hu, Z., 2022. Efficient Sb2S3 solar cells employing favorable (Sb4S6) n ribbon orientation via hydrothermal method. Mater. Lett. 316, 132032.